Supplement of BrO and Br_y profiles over the Western Pacific: Relevance of Inorganic Bromine Sources and a Br_y Minimum in the Aged Tropical Tropopause Layer

Glossary of abbreviations and symbols

Abbreviation	Definition
2D-C	2D-C Hydrometeor Probe
AMAX-DOAS	Airborne MAX-DOAS
AMF	Air Mass Factor
AP1	AMAX-DOAS Acton Pixis covering 330-470 nm
AP2	AMAX-DOAS Acton Pixis covering 440-700 nm
ATTREX	Airborne Tropical TRopopause EXperiment
AWAS	Advanced Whole Air Sampler
BAe-146	British Aerospace 146 aircraft
box-AMF	Air Mass Factor computed in Radiative Transfer Model gridbox
Br	Bromine atom, atomic bromine
BrCl	Bromine chloride
$BrNO_2$	Bromine nitrite
BrO	Bromine monoxide
$BrONO_2$	Bromine nitrate
BrO_x	Active bromine (= Br + BrO)
Br_y	Total inorganic bromine (= Br + Br_2 + BrO + $BrNO_2$ + $BrONO_2$ + HBr + HOBr + BrCl + IBr)
CAST	Coordinated Airborne Studies in the Tropics
CalNex	California Nexus field campaign
CAM-Chem	Community Atmospheric Model with Chemistry
CCD	Charge Coupled Device
CDP	Cloud Droplet Probe
CFC-11	Trichlorofluoromethane
CH_4	Methane
CH_2Br_2	Dibromomethane, methylene bromide
CH_2BrCl	Bromochloromethane
CH_2IBr	Briomoiodomethane
$CHBrCl_2$	Bromodichloromethane
$CHBr_2Cl$	Dibromochloromethane

$CHBr_3$	Bromoform
CHOCHO	Glyoxal
CI	Confidence Interval
CIMS	Chemical Ionization Mass Spectrometry
CO	Carbon monoxide
CO_2	Carbon dioxide
CONTRAST	CONvective TRansport of Active Species in the Tropics
CRDS	Cavity Ring Down Spectrometer
CU	University of Colorado
dSCD	Differential Slant Column Denisty
DOAS	Differential Optical Absorption Spectroscopy
EA	Elevation Angle
FT	Free Troposphere
FWHM	Full width half maximum
GC-MS	Gas Chromatograph - Mass Spectrometer
GEOS CCM	Goddard Earth Observing System with Chemistry-Climate Model
GEOS-Chem	Goddard Earth Observing System with Chemistry model
GEOS-FP	Goddard Earth Observing System Forward-Processing data products
GMAO	Global Modelling and Assimilation Office
GT	Georgia Institute of Technology
GV	NCAR/NSF Gulfstream V aircraft (synonym for HIAPER)
H_2O	Water
HARP	HIAPER Atmospheric Radiation Package
HAIS	Hyper Aircraft Instrumentation Solicitation
HBr	Hydrogen bromide, hydrobromic acid
HCR	Heterogeneous Chemical Regimes
HCHO	Formaldehyde
HEFT-10	HAIS Experimental Flight Test 2010
HIAPER	High-Performance Instrumental Airborne Platform for Environmental Research (synonym for NSF/NCAR GV)
HSRL	High Spectral Resolution Lidar
HOBr	Hypobromous acid
HO_2	Hydroperoxy radical
HO_x	Hydrogen oxide radicals (= OH + HO_2)
IBr	Iodine bromide
ISAF	In Situ Airborne Formaldehyde

IO	Iodine monoxide
J	Photolysis rate
k	Reaction rate
LLS	Longer Lived Species (of organohalogens)
LS	Lower Stratosphere
MAX-DOAS	Multi AXis - DOAS
MBL	Marine Boundary Layer
MU	Manchester University
NASA	National Aeronautics and Space Administration
NCAR	National Center for Atmospheric Research
NIR	Near infrared
NSF	National Science Foundation (USA)
NO	Nitrogen monoxide
NO_2	Nitrogen dioxide
NO_x	Active nitrogen oxides (= NO + NO_2)
O_3	Ozone
O_4	Oxygen collision pair (O_2-O_2)
OH	Hydroxy radical
OVOC	Oxygenated Volatile Organic Compound
PGI	Product Gas Injection (of organohalogens)
PMT	Photon Multiplier Tube
ppb	Parts per billion (nmol mol^{-1})
ppm	Parts per million (µmol mol^{-1})
ppt	Parts per trillion (pmol mol^{-1})
QDOAS	DOAS analysis software
RF	Research flight
RTM	Radiative Transfer Model
SA	Surface Area
SCD	Slant Column Density
SGI	Source Gas Injection (of organohalogens)
SSA	Sea-Salt Aerosol
SZA	Solar Zenith Angle
TL	Transition Layer
TOGA	Trace Organic Gas Analyzer
TTL	Tropical Tropopause Layer
TTL-LMS	Tropical Tropopause Layer – LowerMost Stratosphere

tWPO	tropical Western Pacific Ocean
UHSAS	Ultra-High Sensitivity Aerosol Spectrometer
UTC	Coordinated Universal Time
UTLS	Uppper Troposphere - Lower Stratosphere
VCD	Vertical Column Density
VCSEL	Vertical Cavity Surface Emitting Laser
VSLS	Very Short Lived Species (of organohalogens)
VMR	Volumn Mixing Ratio
VUV	Vacuum Ultra-Violet
WS-CRDS	Wavelength-Scanned CRDS
γ	Surface reaction/uptake probability
θ	Potential temperatue
λ	Wavelength

Jet Cross Case Studies Description

Results from two jet cross flights are included in this work, the flight tracks are shown in Fig. 1. The jet location as crossed in RF15 is also shown. The location of the jet during RF06 is not fully corroborated by measurements as in RF15, but was forecast to be very near the northernmost point of RF06 at 32°N.

The atmospheric context of RF06 is shown in Fig. S5. The data included for modeling starts at 01:16 UTC on 25 January, when the aircraft was at 23.65°N, 148.41°E, and 13.1km altitude. The flight path was NNW almost level at 13.2 km altitude, with small stepwise ascents in the latter portion of the flight. Figure S5 shows that horizontal wind increased as the aircraft approached the subtropical jet stream. At 01:35 UTC the aircraft crossed from the convective TTL to the aged TTL, changes in CO and θ corroborate those in O_3 and H_2O. The aircraft entered the jet at 13.2 km and 28.42°N, horizontal wind peaked just below 70 m s^{-1}. At 02:18 UTC, 32.12°N, 149.90°E, and 13.3 km the GV reversed course, heading SSW continuing to climb. Between 03:20 and 04:00 UTC the aircraft flew at a consistent altitude between 14.3 km and 14.4 km, traveling through the convective TTL transition. The remainder of the flight from 04:00 to 04:56 UTC sampled the more typical convective TTL, including instances of convection.

Figure 3 shows a number of atmospheric tracers for RF15. The data included for modeling start at 00:26Z on 25 February, when the aircraft was at 24.01°N, 145.14°E, and 13.1 km altitude. The aircraft traveled almost due north, with occasional climbs as geopotential altitude gradually decreased. The tropospheric approach of the jet was similar to RF06. The GV transitioned from the convective TTL to the aged TTL at 01:01 UTC, and the jet was first encountered at 01:12 UTC, reaching peak windspeed near 80 m s^{-1}. A second component of the jet with the slower windspeed (~65 m s^{-1}) was similar to the most stratospheric of the air masses encountered during RF 06: i.e., 100 ppb < O_3 < 200 ppb, and H_2O/O_3 ~ 0.02 ppm/ppb, characteristic of the TTL. At 01:35 UTC, 32.92°N and 12.9 km, O_3 increased sharply indicating the transition into the stratosphere, and windspeed decreased as the GV crossed into the

middleworld LS. Although not shown on Fig. 4, this transition was marked the first time CFC-11 deviated consistently from tropospheric values, indicating long residence at high altitude with photochemical processing of the sampled air masses. At 02:25 UTC the aircraft encountered a second rapid O_3 gradient, traveled to the maximum flight latitude of 40.13°N, climbed from 12.6 to 12.9 km, reversed course to due south, and transitioned from the middleworld to the overworld at 02:32 UTC. At 03:26 UTC at 13.5 km and 33.14°N the GV crossed from the overworld back to the aged TTL, skipping the LS middleworld. Nothing analogous to the convective TTL "transition" in RF06 was encountered during RF15. Instead there was a smooth change from the aged TTL to the convective TTL at 4:21 UTC. Instances of convection were first encountered at 04:38 UTC.

Gas Phase Measurements Used to Constrain the Box Model

The measurements used to constrain the box model to infer Br_y from BrO are summarized in Table 1. The handling of AMAX-DOAS data is described in detail in the main text (Sect. 2.1). Other data were used in the following manner with specific exceptions outlined here after. Where data were below detection limit the nominal value of ½ the detection limit was used. With the exception of NO_2 discussed below no parameter impacted Br_y partitioning significantly at the relevant level when near its respective detection limit. Where data was quality flagged it was interpolated across.

High frequency data ~1 Hz, namely Chemiluminescence (NO, NO_2, and O_3), HARP photolyses, ISAF HCHO, PICARRO CH_4, UHSAS aerosols, Aerolaser VUV fluorescence CO, and state parameters were averaged over the relevant interval. For profiles this was at the 500 m of flight altitude, for level flight relevant periods of ~ 5 minutes. Lower frequency data, namely AWAS and TOGA were interpolated to the mean; for level flight they were interpolated in altitude, for level flight they were interpolated in time.

Early research flights including the profile case studies had incomplete data coverage. In particular, AWAS data were not available for RF03 and RF04; PICARRO and Aerolaser VUV fluorescence for RF03; and ISAF for a portion of RF04. For AWAS measurements with the exception of ethane TOGA measurements were available which were substituted. For ethane, AWAS ethane was compared to Picarro methane for tropical profiles from RF05, RF06, and RF07 to obtain an average ratio of ethane:methane of 1.59×10^{-4}:1. This ratio was used to obtain an ethane concentration from the methane concentration for RF03 and RF04. For RF03 where CO and CH_4 were not available the mean profiles for each species from GEOS-Chem were used. For the portion of RF04 where ISAF HCHO is not available, TOGA HCHO is substituted.

AWAS and TOGA measure some of the same species used in the box model (propane, isobutane, n-butane, and benzene). AWAS data were used for these species for level flight data, where detection limits give more complete coverage in stratospheric air; while TOGA data were used for the profile case studies, where it has a higher frequency and more consistent coverage, further AWAS data is unavailable for RF03 and RF04. The agreement between TOGA and AWAS differs among the species measured, but very rarely exceeds their respective reported errors. CFC-11 and bromocarbon measurements were examined to further understand differences, corroborating the level of agreement for hydrocarbons. The species used in the box model (propane, isobutane, n-butane, and benzene) impact Br_y partitioning via alkylperoxy radicals which do not impact sufficiently by differences to have a significant impact.

NO_2 can have a significant impact on Br_y partitioning, not only via direct reaction but indirectly through impacts on HO_x. At high altitude, some Chemiluminescence measurements of NO_2 were less than zero. These data were averaged with GEOS-Chem NO_2 in order to have a physically meaningful value but remain generally consistent with the observations of NO_2 below the levels elsewhere. Further for the RF15 case study, the Leighton ratio deviates significantly from model predictions, and AMAX-DOAS NO_2 was used to constrain the box model for this flight (Fig. S1). In the TTL, despite different measurement principles, AMAX-DOAS and Chemiluminescence NO_2 were roughly consistent and generally elevated relative to box models and global model predictions. In the stratosphere high ambient O_3 may impact Chemiluminescence measurements of NO_2, which deviated further from model predictions. AMAX-DOAS NO_2, however, while elevated relative to box models, is roughly consistent with CAM-Chem.

Gas Phase Measurement Techniques

Advanced Whole Air Sampler (AWAS)

The Advanced Whole Air Sampler (AWAS) consists of modules of 12 custom stainless-steel 1.3 L sampling canisters. Typically five modules (60 canisters) were collected in a flight, sampling was determined by an inflight operator. Sample flow was altitude dependent and varied between 5 slpm and 30 slpm. These samples can then be analyzed for a wide variety of hydrocarbons, halocarbons, organonitrates, and other species.

Samples are analyzed on the ground after flight using a Markes Canister Interface 5 (CIA) and a Unity II system connected to an Agilent 5975 GC/MSD. Samples were dried and pre-concentrated on Markes Ozone Precursor Trap (Markes UT17O3P-2S). Samples of 800 scc are thermally desorbed at 300 °C and split between two GC, 1) a 30 m x 0.25 mm x 5 micron Alumina 10 PLOT column (HP-AL/S, Agilent Technologies) followed by a 1 m GasPro with a flame ionization detector, and 2) a 20 m x 0.2 mm x 1.12 μm DB-624 column (128-1324, Agilent Technologies) to both an electron capture detector and the MSD. Further details on sampling and analysis can be found in Andrews et al. (2016) and Navarro et al. (2015). Calibration was done every five samples against a cryogenically collected standard which in turn is calibrated by a procedure described in Schauffler et al. (1999).

Chemical Ionization Mass Spectrometer (CIMS)

The Georgia Tech CIMS (GT CIMS) measured gas phase bromine species (BrO, and HOBr +Br_2), it is more fully described in Chen et al. (2016). In brief the instrument sampled air from outside the GV through a Teflon tube, ionized by water-iodide clusters in a flow tube, ions are further processed in a collisional dissociation chamber (CDC), guided by an octopole field, and then analyzed on a mass spectrometer. Air was sampled at 5.2 standard litres per minute (sLpm). HOBr is known to process to Br_2 on the inlet and the sum of the detected signals is used as a result. Up to 1.7 sLpm of this was sampled off the line by an automatic variable orifice with the remainder exhausted to maintain a constant 50 Torr pressure in the flow tube. CH_3I at a few ppm in 2.9 sLpm N_2 buffer gas was flowed over a ^{210}Po source to generate iodide and then mixed with 0.1 sLpm humidified N_2 to provide hydrated iodide ions in the flow tube. Gas phase bromine species reacted with these to form clusters. Water was removed from the clusters by the electric field in the CDC which in addition has a vacuum maintained independent of the flow tube. The core ions,

dehydrated iodide-analyte clusters, were then guided by the octopole then selected and detected on the quadrapole. The consistency of detected signals from the bromine isotopes ^{79}Br and ^{81}Br was used as a data quality check.

Chemiluminescence

Two instruments measure the trace gasses NO, NO_2, and O_3 using chemiluminescence of the $NO+O_3$ reaction. The first is a two channel detector for NO and NO_2. Air sampled from outside the aircraft is split onto the channels. On the NO_2 channel, UV light at 395 nm is used to photolyse NO_2 to NO. Both channels are then reacted with O_3 from two ozonizers, PMT detectors measure the emission of the NO_2^* product at 600 nm - 2800 nm. NO in N_2 is used as a calibration gas. The Fast-O_3 detects O_3 using a similar system. Ambiently sampled O_3 is reacted with reagent grade (> 99%) NO, and the same product is detected using a PMT.

In Situ Airborne Formaldehyde (ISAF)

The In Situ Airborne Formaldehyde (ISAF) instrument utilizes laser induced fluorescence (LIF) at 353.16 nm to selectively measure formaldehyde in air collected off an inlet. A pulsed tunable fiber laser is rapidly tuned on and off of the rotational resonance feature which minimizes interference and serves as a real time monitoring of background. The resulting fluorescence is monitored by a PMT. The instrument was calibrated by standard addition of formaldehyde before and after the campaign. A more complete description of ISAF is available in Cazorla et al. (2015).

Piccaro CO_2/CH_4 Flight Analyzer

The Piccaro G1301-c Methane/Carbon Dioxide Analyzer utilizes Wavelength-Scanned Cavity Ring Down Spectroscopy (WS-CRDS) driven by an NIR laser. Gas sampled from outside the aircraft is circulated through a cavity with an effective path length of 20km. The instrument has been ruggedized for aircraft operation and utilizes a patented, high-precision wavelength monitor to minimize interference from other trace gasses. Only methane is used in the box model.

Trace Organic Gas Analyzer (TOGA)

TOGA consists of a custom GC-MS system which measures a variety of species including hydrocarbons, halocarbons, and non-acid oxygenated volatile organic compound (OVOC). Samples are collected off the main inlet line at 15 ml per minute for 35 seconds through a series of three cold traps, then run on a custom GC with a Restek MXT-624 column. Effluent from the GC is analyzed on an Agilent Technologies 5973N quadrupole mass spectrometer system ruggedized for aircraft use by substitution of the vacuum pump with a Varian Model V301 NAV. Total time to process a single sample is 2.0 minutes. Further details on TOGA can be found in Andrews et al. (2016) and Apel et al. (2003, 2010, and 2015).

VUV Carbon Monoxide

The VUV carbon monoxide instrument generates vacuum UV light through RF plasma discharge, this is bandpass filtered (8 nm FWHM) around 150 nm to excite CO fluorescence while minimizing interference from water. Fluorescence is monitored by PMT. A more complete description of the instrument is available in Gerbig et al. (1999).

Particle Measurements

2D-C Hydrometeor Probe (2D-C)

The 2D-C Hydrometeor Probe is customized through installation on high speed electronics and installation of a 64 element photodiode array from a product originally produced by Particle Measuring Systems Inc. An open path between two arms perpendicular to flight is illuminated and images of individual particles are imaged on the 64 element array. Particles with diameters between 62.5 μm and 1587.5 μm are detected, though the depth of field limits sensitivity to smaller particles. Furthermore, the arms are known to shatter larger particles, though they have been designed to minimize this effect. 2D-C images were not directly referenced, rather, a processed data product classifying particles into 60 size bins was used an indication of cirrus clouds. Calculations of cirrus ice surface area were used to inform box model sensitivity studies as discussed in Section 2.3.1.

Cloud Droplet Probe (CDP)

The Cloud Droplet Probe (CDP) manufactured by Droplet Measurement Technologies, Inc. utilizes forward scattering to detect particles in the range of 2 μm to 50 μm in size. A diode laser is run across an open path perpendicular to flight. Particles which pass through the depth of field in the open path are counted and sized into one of 30 bins in the size range. A more complete description of the CDP is available in Lance et al. (2010). CDP data was referenced and utilized in sensitivity studies but not ultimately utilized in the box model. This is discussed in Section 2.3.1.

Ultra-High Sensitivity Aerosol Spectrometer (UHSAS)

The wing-mounted Ultra-High Sensitivity Aerosol Spectrometer utilizes a laser at 1054 nm to optically detect particles along the GV flight path. The instrument is sensitive to particles in the 0.060 μm to 1.0 μm diameter range and records particles into 99 roughly logarithmic size bins covering this size range. During CONTRAST, however, frequent noise necessitated discarding the smallest twelve bins, making 0.084 nm the effective lower bound of the probe. A more complete description of a ground-based version of the UHSAS may be found in Cai et al. (2008). UHSAS data were used in the box model for all flights to compute aerosol surface area for heterogeneous reactions. Furthermore, sensitivity studies were conducted increasing diameter by a factor of two based on the results of a previous optical closure study (Volkamer et al., 2015); this is further illustrated for the RF03 profile in Fig. S3. Increasing particle size by a factor of two leads to general agreement between AMAX-DOAS retrieved extinction using O_4 and extinction computed from UHSAS using Mie theory above ~3 km. In the boundary layer even increasing particle size and including supermicron particles from the CDP still yields sub-Rayleigh scattering at 360 nm, significantly below the extinction measured by AMAX-DOAS.

Meteorological Parameters

HIAPER Airborne Radiation Package (HARP)

The HIAPER Airborne Radiation Package (HARP) includes CCD spectroradiometers, and irradiance detectors measuring upwelling and downwelling radiation. Detectors are mounted on an actively motion stabilized platform to maintain horizontal stability despite aircraft deviations of up to 5 degrees. Data from the spectroradiometers was used in this work. These measure actinic flux in the range of 280 nm to 680 nm. These are then processed using a modified version of the Tropospheric Ultraviolet and Visible (TUV) radiative transfer model to generate photolysis frequencies for a wide variety of species including O_3, NO_y species, small aldehydes and ketones, organonitrates, Br_y species, and Cl_y species. These were used for all photolysis reactions used in the box model. Further details on HARP can be found in Pilewskie et al. (2003) and Shetter and Müller (1999).

Vertical Cavity Surface Emitting Laser (VCSEL) hygrometer

The Vertical Cavity Surface Emitting Laser (VCSEL) a tunable NIR laser based hygrometer measuring absolute water concentration. The instrument achieves a high dynamic range by monitoring two different water absorptions at two similar wavelengths, a 'strong' absorption at 1854.03 nm and a 'weak' one at 1853.37 nm. The cavity has a physical extent of 14.95 cm which is passed 25 times for a path length of 3.74 m. Measurement is typically done by second harmonic detection except in the mid-troposphere where the second harmonic of the strong band is nonlinear and direct absorption is used. Further information on VCSEL is available in Zondlo et al. (2010).

GV State Parameters

The National Science Foundation/National Center for Atmospheric Research Gulfstream V (NSF/NCAR GV) aircraft records a wide variety of state parameters. Some of these such as temperature and pressure were utilized in the box model. Others such as θ and horizontal wind speed were used as context for model results. Finally, in order to match the spatial scale probed by in situ sensors and remote sensors, the median photon sampled by the AMAX-DOAS was calculated by radiative transfer, and the in situ data were averaged, and shifted in time to match DOAS sampled air volumes. For the horizontal case studies – RF06 and RF15 – the lateral wind speed was strong, such that the aircraft heading and the measurement vector are offset by approximately 5°. No further corrections were made to attempt account for this perpendicular offset. However, the air masses probed remotely are blown towards the aircraft, and the time delay at which the in situ data were averaged partially account for this offset.

Supplemental Tables and Figures

Table S1: Parameters input and output for optimal estimation.

Parameter	**RF03**	**RF04**	**RF07**
p, T, H_2O, NO_2, O_3, O_4	in situ data where available, model above flight altitude		
Aerosol Properties			
AOD (360 nm)	0.304	0.272	0.231
g-parameter	0.77 (0-2.4 km), 0.72 (2.4-6.0 km), 0.7 (>6.0 km)		
Single Scattering Albedo	0.98		
Surface Albedo	0.05		
Inversion Properties			
ab initio profile	1.0 ppt constant tropospheric mixing ratio		
ab initio error	2,000%	10,000%	10,000%
Inversion Grid	500 m (aerosol at 200 m resolution)		
Degrees of Freedom	18.2	17.2	26.9
Mean Averaging Kernel	0.728	0.953	0.962

Table S2: Comparisons of partial and total tropospheric HBr VCDs predicted by different models.

Altitude	HBr VCD $\times 10^{12}$ (box-model -case 1)	HBr VCD (GEOS-Chem no SSA source)	HBr VCD (GEOS-Chem w/ SSA source)	HBr VCD (CAM-chem)
MBL	0.0 (0.0, 0.0)	0.1 (0.0, 0.8)	5.2 (0.8, 9.0)	0.8 (0.4, 2.9)
TL	0.0 (0.0, 0.0)	3.1 (1.5, 5.4)	18.9 (9.3, 28.4)	3.1 (1.1, 6.5)
Lower FT	0.0 (0.0, 0.1)	6.2 (3.7, 9.2)	14.6 (7.6, 27.3)	9.0 (3.9, 17.0)
Mid FT	0.3 (0.1, 0.8)	1.5 (0.9, 2.6)	2.3 (1.0, 4.4)	2.7 (0.7, 5.2)
Upper FT	2.7 (2.1, 5.2)	2.2 (1.6, 2.7)	3.4 (2.6, 4.1)	1.0 (0.0, 1.7)
TTL	0.1 (0.0, 0.8)	1.0 (0.6, 1.3)	1.5 (0.9, 1.9)	0.3 (0.0, 0.9)
Troposphere	3.2 (2.1, 6.8)	14.1 (8.3, 22.0)	46.0 (22.2, 75.2)	17.0 (6.2, 34.3)

Values in parentheses are the 1st and 3rd quartile. Global models have much more HBr, especially in the lower atmosphere. This is likely related to the handling of HBr uptake as discussed in the text. The global models also show an HBr minimum in the upper FT and TTL, which is the box model maximum.

Table S3: Summary of BrO and Br_y over the tWPO.

Region	BrO ppt	Br_y ppt			
		case 0	case 1	case 2	case 3
MBL	1.7 (0.2, 1.0, 3.8, 4.4)	13.8 (2.0, 5.5, 30.2, 35.0)	13.8 (2.0, 5.5, 30.2, 35.0)	13.8 (2.0, 5.5, 30.2, 35.0)	13.8 (2.0, 5.5, 30.2, 35.0)
TL	1.2 (0.3, 0.6, 1.3, 1.8)	5.8 (1.9, 3.4, 8.7, 12.4)	5.8 (1.9, 3.4, 8.7, 12.4)	5.8 (1.9, 3.4, 8.7, 12.4)	5.8 (1.9, 3.4, 8.7, 12.4)
lFT	0.7 (-0.1, 0.4, 0.9, 1.2)	2.8 (0.9, 1.6, 5.0, 6.1)	2.8 (0.9, 1.6, 5.0, 6.1)	2.8 (0.9, 1.6, 5.0, 6.1)	2.8 (0.9, 1.6, 5.0, 6.1)
mFT	0.6 (0.1, 0.5, 1.0, 1.3)	3.6 (0.8, 1.7, 5.1, 6.0)	1.6 (0.8, 1.2, 3.5, 4.1)	1.6 (0.7, 1.2, 3.4, 3.9)	1.6 (0.7, 1.2, 3.4, 3.9)
uFT	0.6 (0.2, 0.3, 0.7, 0.8)	6.2 (2.1, 2.6, 7.6, 10.9)	2.1 (0.8, 1.5, 3.1, 6.2)	1.7 (0.5, 0.7, 2.1, 2.3)	1.7 (0.5, 0.7, 2.1, 2.3)
cTTL	0.9 (0.3, 0.5, 1.1, 1.1)	4.8 (2.9, 4.0, 6.5, 10.5)	3.3 (1.7, 2.6, 4.2, 5.3)	2.6 (1.4, 1.8, 3.1, 3.4)	2.6 (1.4, 1.8, 3.1, 3.4)
aTTL	1.2 (0.7, 0.9, 1.8, 1.9)	2.7 (1.7, 2.1, 3.6, 4.2)	2.7 (1.6, 2.0, 3.5, 4.1)	2.6 (1.6, 2.0, 3.4, 3.9)	2.6 (1.6, 2.0, 3.2, 3.7)
LS	3.1 (2.6, 2.8, 3.2, 3.3)	6.9 (5.5, 6.5, 7.5, 8.2)	6.8 (5.5, 6.4, 7.5, 8.2)	6.9 (5.5, 6.5, 7.5, 8.2)	6.0 (4.9, 5.7, 6.5, 7.0)

Values in table are reported as follows: median, (1^{st} decile, 1^{st} quartile, 3^{rd} quartile, 9^{th} decile). Air masses are classified as elsewhere, see Sects. 3.1 and 3.2.

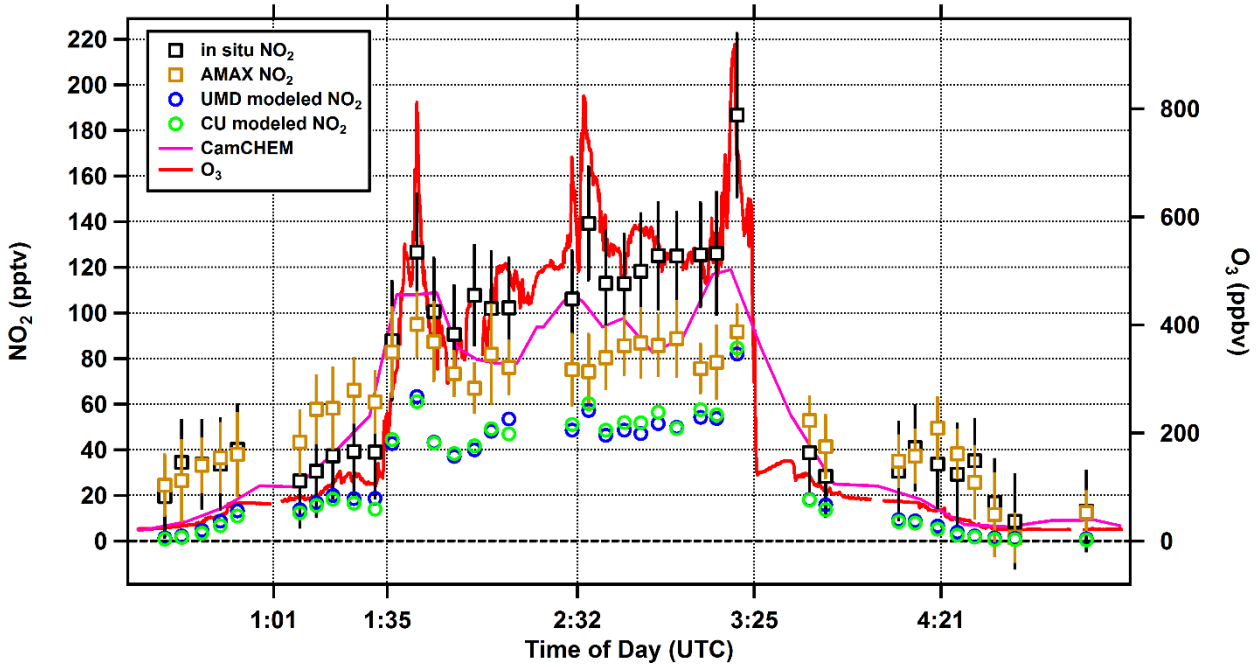

Figure S1: Comparison of NO_2 between (black) in situ NO_2, (gold) DOAS NO_2, (green) NO_2 modeled using the box model constrained by in situ measured NO, (blue) NO_2 modeled by a second box model operated at the University of Maryland, constrained by in situ measured NO. AMAX-DOAS and in-situ NO_2 agree within error bars in the troposphere. However, DOAS is systematically lower than in-situ NO_2 in the stratosphere, where high O_3 is believed to introduce a high bias to the in situ NO_2 measurements; O_3 is shown in red on the right axis. DOAS NO_2 was used to constrain the box model in this case study.

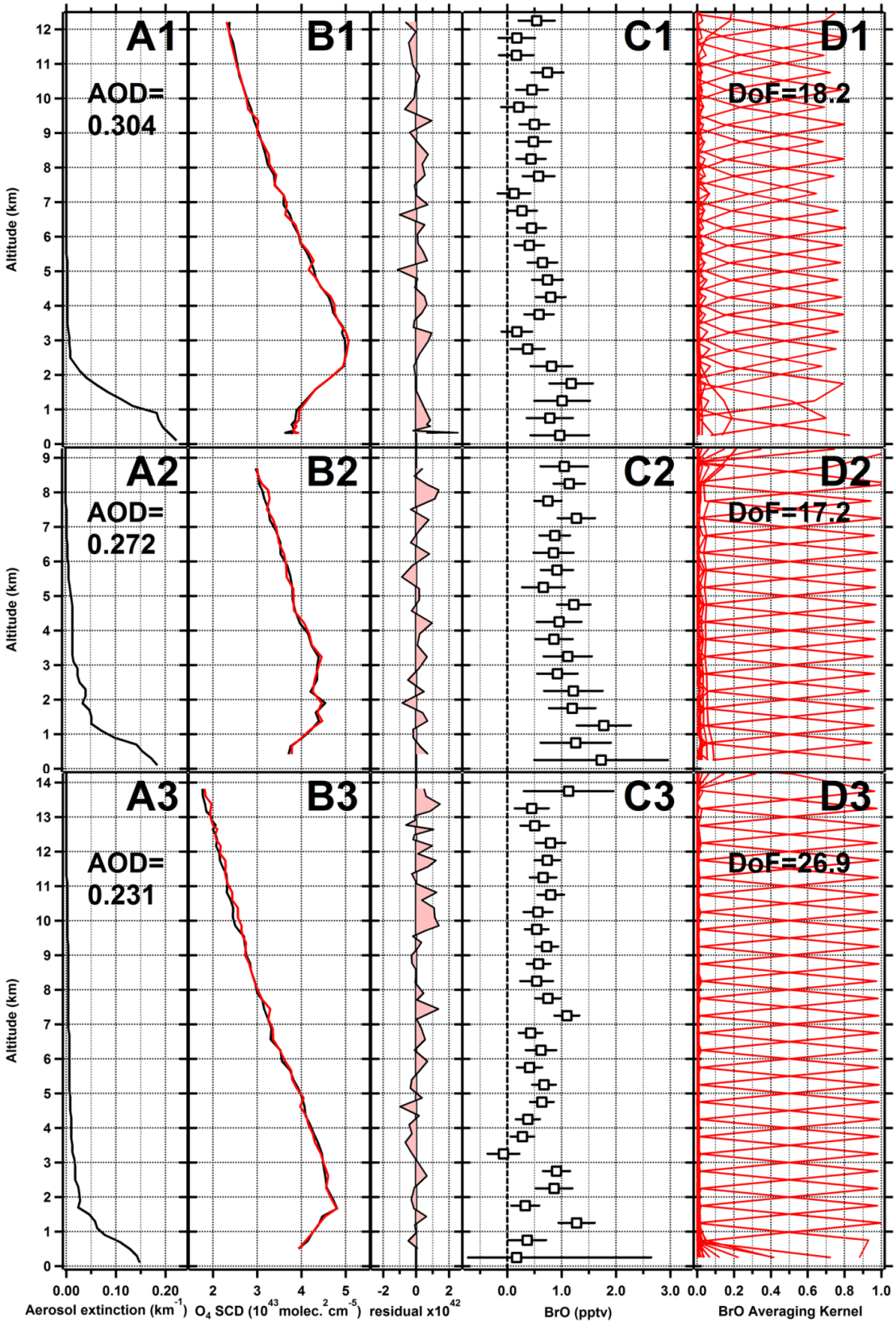
A1
AOD=
0.304
B1
C1
D1
DoF=18.2
A2
AOD=
0.272
B2
C2
D2
DoF=17.2
A3
AOD=
0.231
B3
C3
D3
DoF=26.9
Altitude (km)
Aerosol extinction (km-1)
O4 SCD (1043 molec.2 cm-5)
residual x1042
BrO (pptv)
BrO Averaging Kernel

Figure S2: Optimal estimation of BrO profiles for case studies 1) RF03, 2) RF04, 3) RF07. Panels A: the retrieved aerosol extinction profile at 360 nm, the aerosol optical depth is integrated over the column retrieved assuming zero above maximum flight altitude. Panels B: left subpanel in black measured O_4 SCDs, in red modeled O_4 SCDs, right subpanel the residual (modeled-measured), individual residuals are within $\pm 2 \times 10^{42}$. Panels C: The BrO profiles retrieved by optimal estimation, error bars include fit error, and optimal estimation errors. Panels D: averaging kernels for the BrO optimal estimation. Sharp peaks near 1 indicate independent information in each altitude bin. The Degrees of Freedom (DoF) is the trace of the matrix here truncated to flight altitudes.

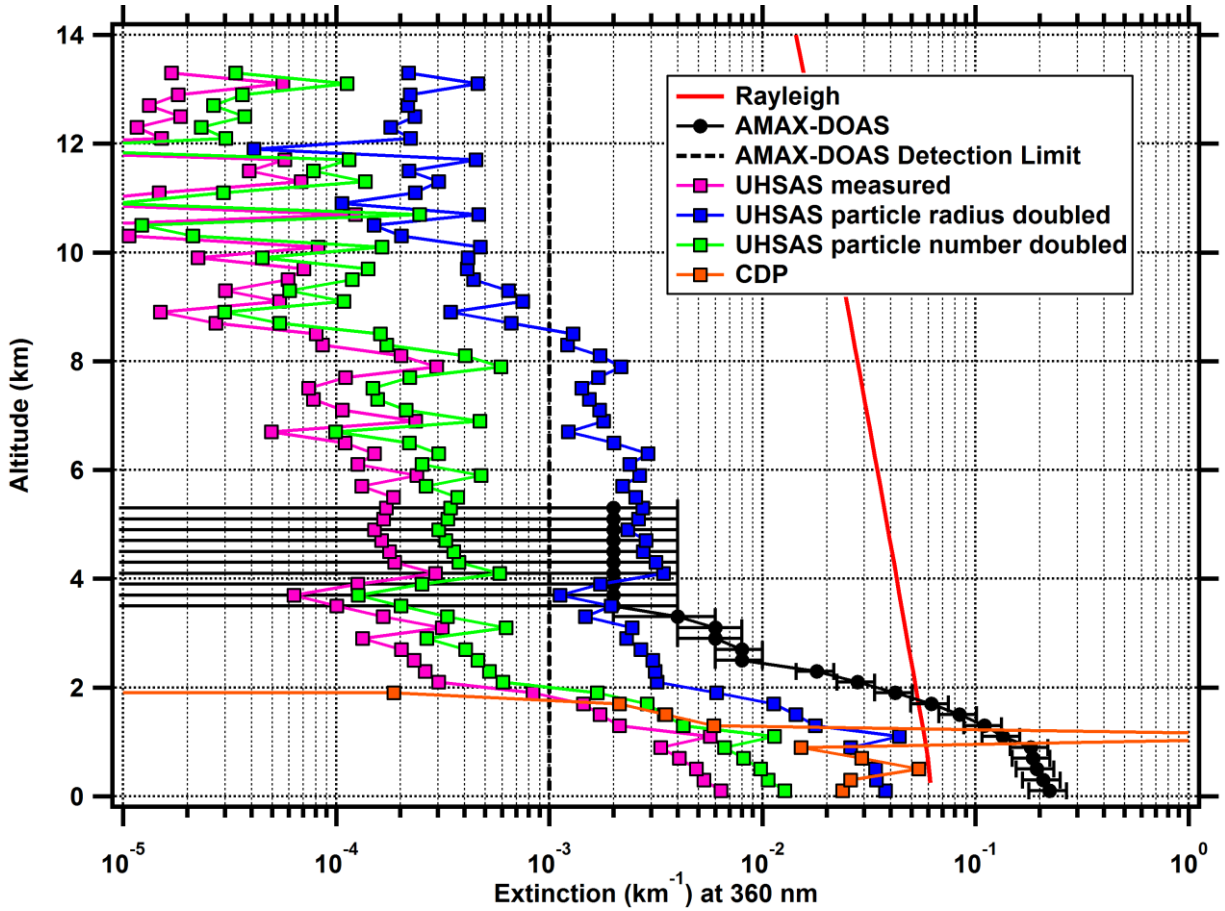

Figure S3: Comparison of aerosol extinction at 360 nm for the RF03 case study profile. AMAX-DOAS extinction is retrieved based on O_4 dSCDs. Particle instrument extinctions are determined by using Mie theory with measured particle size distributions and concentrations as input. Consistent with the findings in Volkamer et al. (2015) measured size distributions do not reproduce the observed extinction and are sub-Rayleigh even in the boundary layer. Increasing particle size improves agreement.

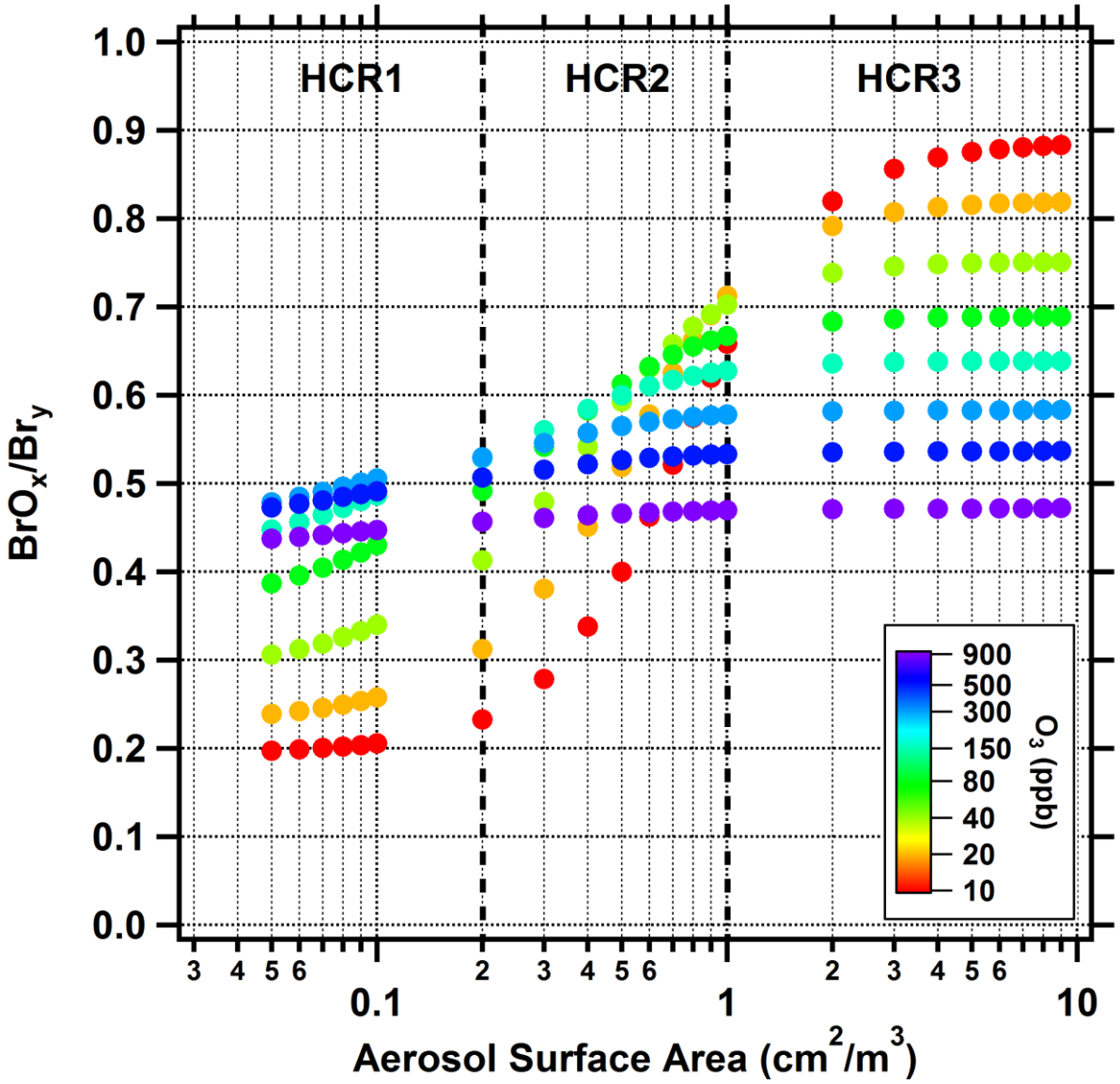

Figure S4: Sensitivity of the BrO_x/Br_y ratio to SA and O_3, under conditions typical of the upper troposphere. (dashed vertical lines) the heterogeneous chemical regimes (HCR, see Sect. 2.3.1). The decreasing HBr fraction with increasing O_3 is visible in HCR1, and is a result of lower bromine atom concentrations (and thus HBr formation rates). HCR2 exhibits the largest sensitivity at low/moderate O_3, typical of the upper FT (uFT) and convective TTL (cTTL). In HCR3 the ratio is largely insensitive to SA, but strongly depends on O_3.

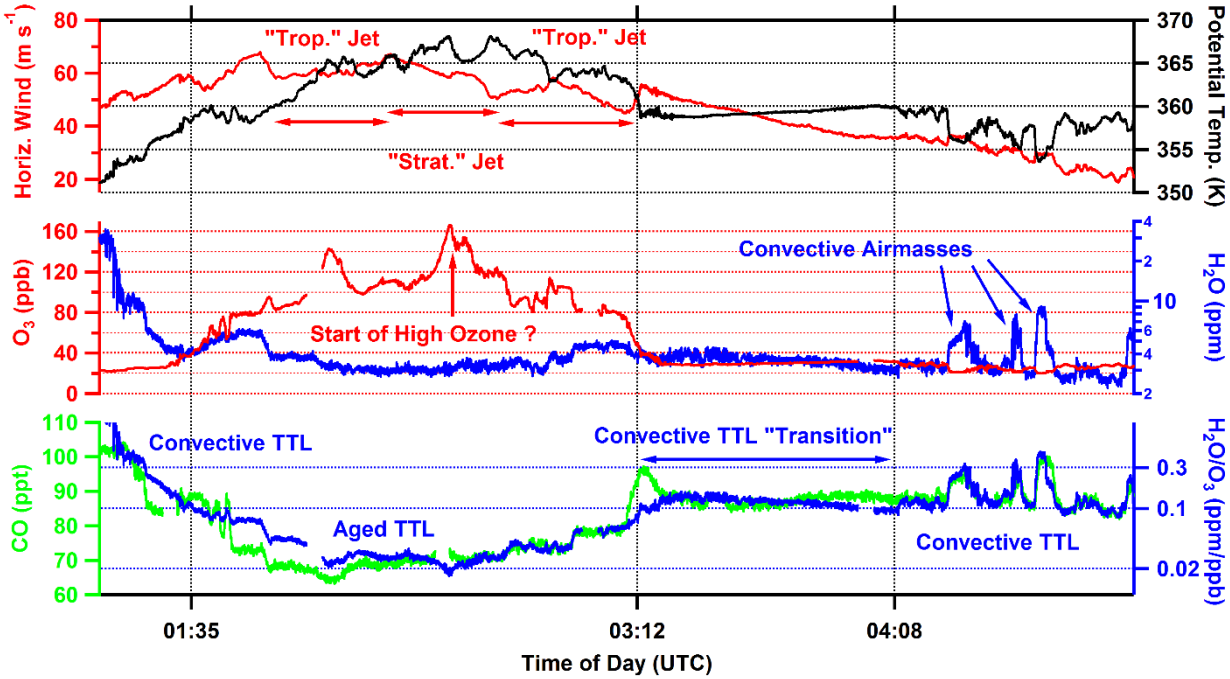

Figure S5: Same as Fig. 3 for RF06.

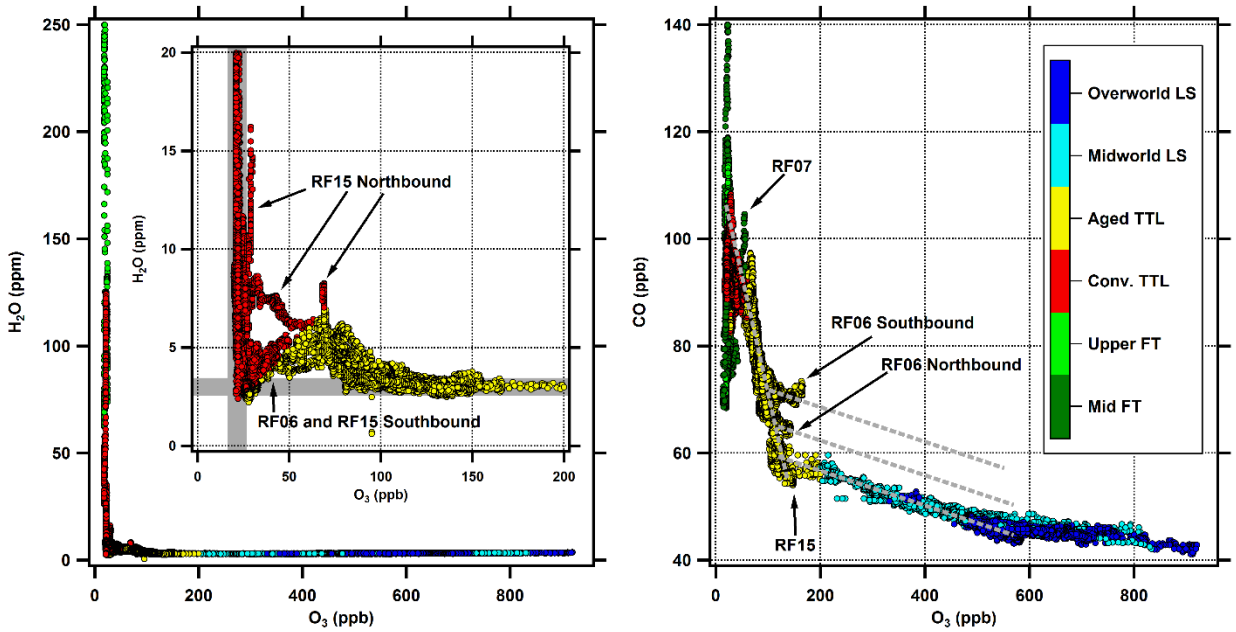

Figure S6: Air mass classification in the context of tracer-tracer classification schemes. Left panel, the scheme from Pan et al., 2014. Air masses that have neither stratospheric H_2O nor tropospheric O_3 (outside the grey regions) are in the TTL. Under such a scheme the convective TTL includes tropospheric air and the aged TTL includes stratospheric air. Right panel, the scheme from Chen et al., 2016, which defines a TTL-LMS transition where the slope between CO and O_3 is -0.4, this generally corresponds to the aged TTL in this work, but also includes portions of the convective TTL and a low altitude filament from RF07. Some aged TTL air masses fall on parallel lines with a CO/O_3 slope of -0.03 consistent with the stratosphere in the Chen et al. scheme.

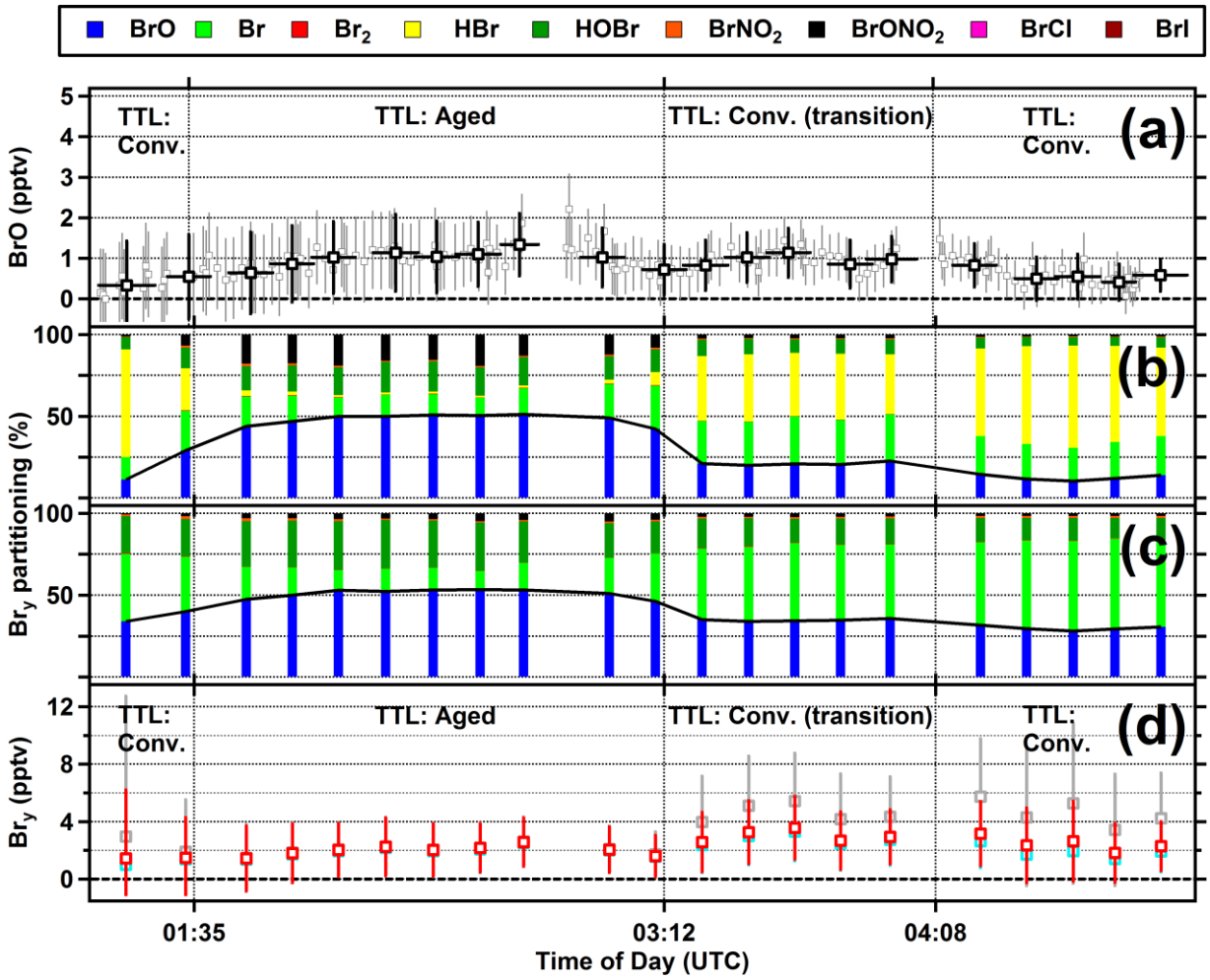

Figure S7: Same as Fig. 4 for RF06.

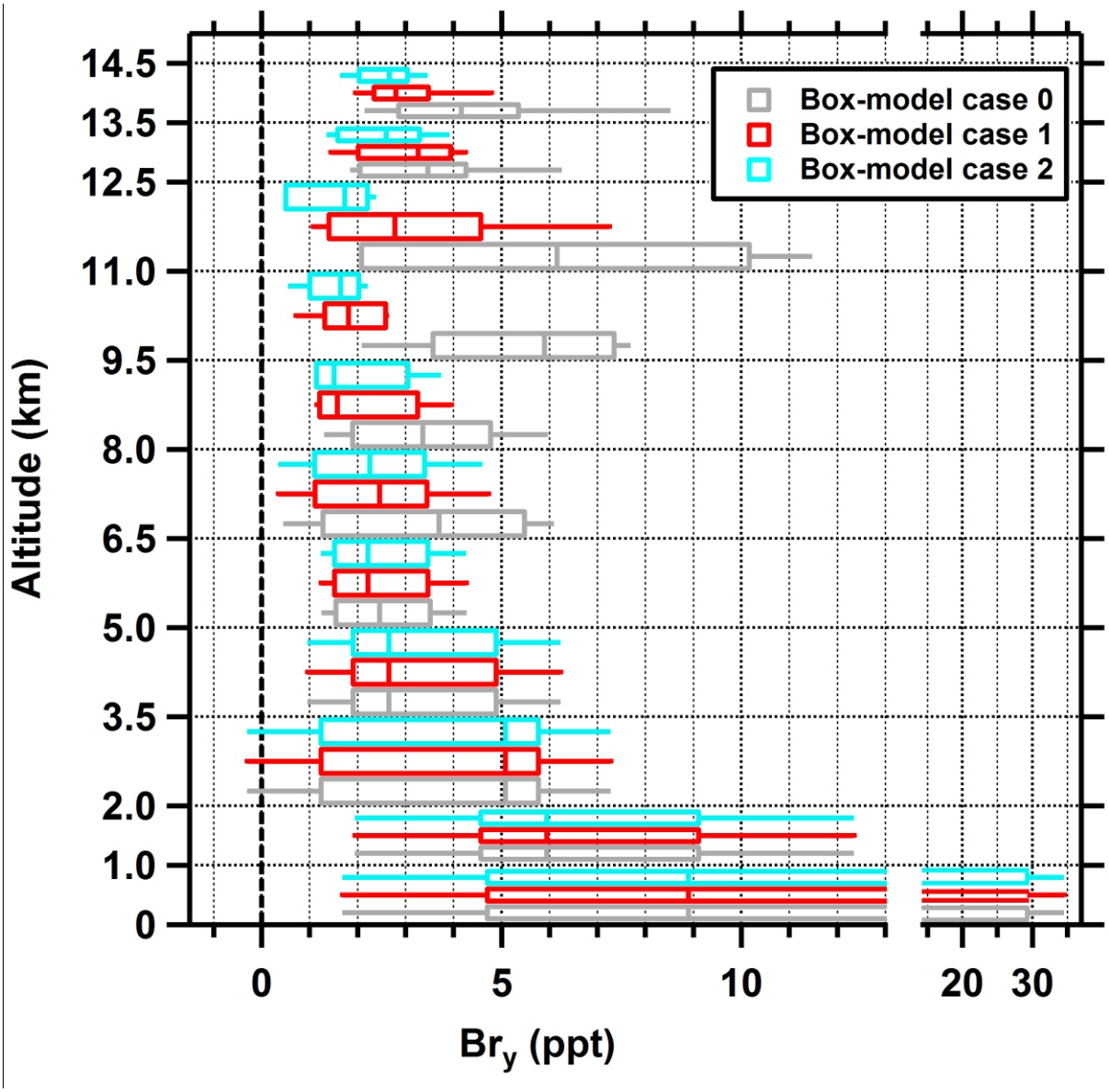

Figure S8: Comparison of modeled Br_y for different box model cases: (grey) case 0, (red) case 1, and (cyan) case 2. Boxes indicate the 25th and 75th percentiles and whiskers indicate the 10th and 90th percentiles. All statistics are computed across the altitudes indicated by the horizontal dashes. The different cases are offset vertically in each box for better visualization.

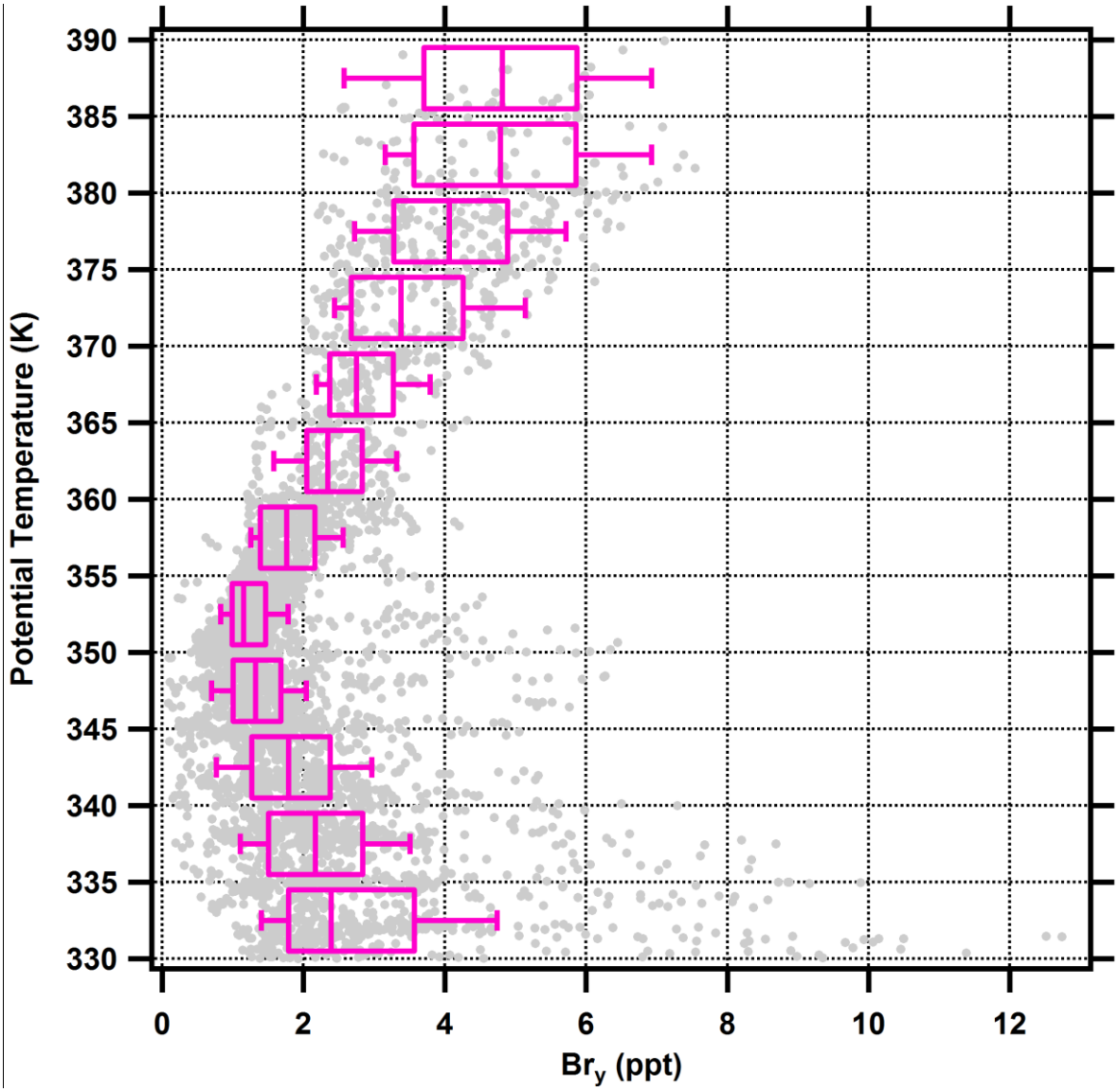

Figure S9: Br$_y$ from CAM-chem for the flights discussed in this work. Grey points in background are individual data points from the extraction, red boxes represent medians, 25th and 75th percentiles, whiskers indicate 10th and 90th percentiles. Consistent with the observations, a Br$_y$ minimum is found in the UTLS, though unlike the observations, at lower θ. CAM-chem has a median (quartile range) of 1.2 (1.0, 1.5) ppt Br$_y$ near 350-355 K, and 2.3 (2.0, 2.8) ppt for 360-365 K. The median and quartile range are consistent with the observed Br$_y$ minimum for 360-365 K, but less Br$_y$ is predicted at lower θ.

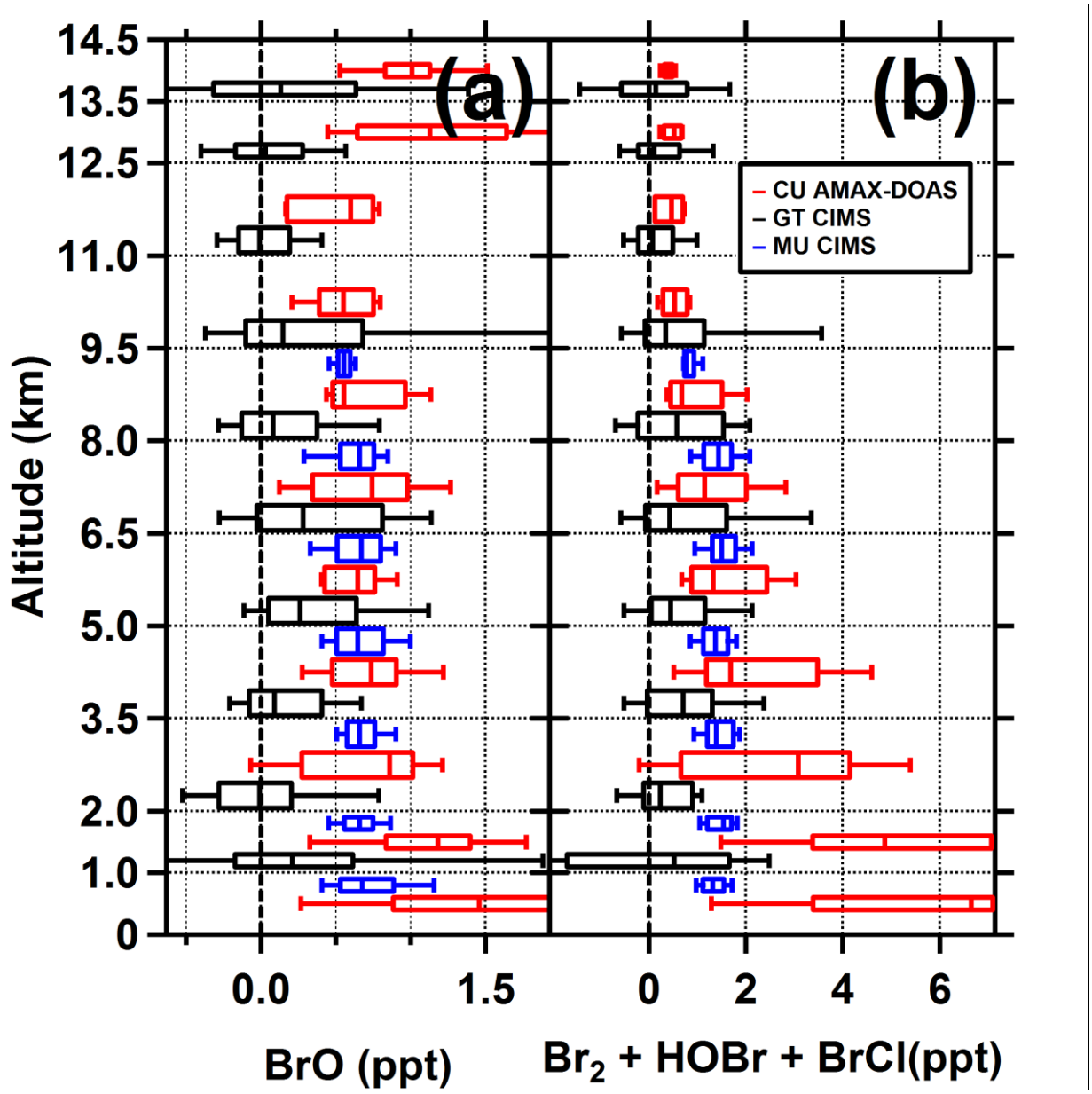

Figure S10: Comparison of bromine measurements by the CU Boulder AMAX-DOAS (blue), Georgia Tech CIMS (Chen et al., 2016) (black) aboard the NSF/NCAR GV during CONTRAST, and the Manchester University CIMS (Le Breton et al., 2017) (red) aboard the FAAM aircraft during CAST. Data are presented as box and whisker plots, where boxes show the interquartile range and median, and whiskers show the 10th and 90th percentile. (a) BrO measurements. Data for the CONTRAST instruments are filtered to exclude stratospheric data (using the LS definition described in the main text). (b) Other Br$_y$ species. Manchester reports Br$_2$, HOBr, and BrCl separately, these are added and statistics gathered on the resulting sum. Georgia Tech reports a single value for the sum of Br$_2$ and HOBr. AMAX-DOAS values are inferred using the box model (case 1), and taken as the sum Br$_2$+HOBr (the model was run with zero chlorine and hence zero BrCl).